

Target-oriented Domain Adaptation for Infrared Image Super-Resolution

Yongsong Huang^{1,2*}, Tomo Miyazaki¹ *Member, IEEE*

Xiaofeng Liu² *Member, IEEE*, Yafei Dong², Shinichiro Omachi¹ *Senior Member, IEEE*

¹ Graduate School of Engineering, Tohoku University, Sendai, Japan

² Harvard Medical School, Harvard University, Boston, MA, USA

Abstract

Recent efforts have explored leveraging visible light images to enrich texture details in infrared (IR) super-resolution. However, this direct adaptation approach often becomes a double-edged sword, as it improves texture at the cost of introducing noise and blurring artifacts. To address these challenges, we propose the Target-oriented Domain Adaptation SRGAN (DASRGAN), an innovative framework specifically engineered for robust IR super-resolution model adaptation. DASRGAN operates on the synergy of two key components: 1) Texture-Oriented Adaptation (TOA) to refine texture details meticulously, and 2) Noise-Oriented Adaptation (NOA), dedicated to minimizing noise transfer. Specifically, TOA uniquely integrates a specialized discriminator, incorporating a prior extraction branch, and employs a Sobel-guided adversarial loss to align texture distributions effectively. Concurrently, NOA utilizes a noise adversarial loss to distinctly separate the generative and Gaussian noise pattern distributions during adversarial training. Our extensive experiments confirm DASRGAN's superiority. Comparative analyses against leading methods across multiple benchmarks and upsampling factors reveal that DASRGAN sets new state-of-the-art performance standards. Code are available at <https://github.com/yongsongH/DASRGAN>.

1. Introduction

IR imaging plays a pivotal role in a wide range of applications, including medical diagnostics [1, 2], target detection [3], remote sensing [4], and autonomous driving [5]. It offers unique pattern information otherwise unattainable through other means. However, generating high-quality IR images remains a formidable challenge, largely due to constraints in imaging systems and adverse conditions, such as limited line-of-sight and atmospheric fog [6, 7]. In re-

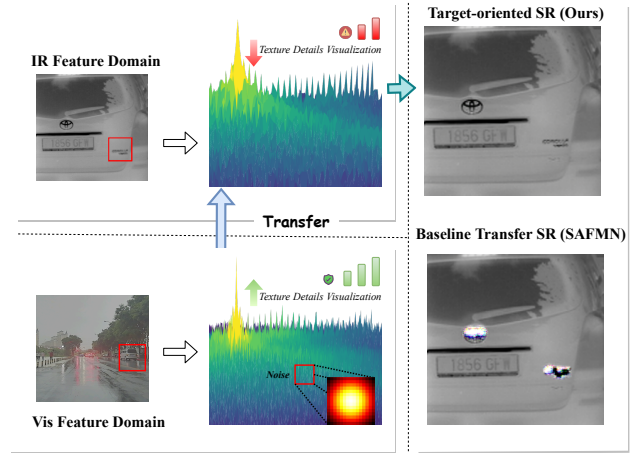


Figure 1. Our proposed SR model advances target-oriented domain adaptation by overcoming the constraints inherent in existing baseline approaches [9]. Specifically, our model is designed to counteract degrading factors such as Gaussian blur in the visible spectrum, thereby facilitating a more effective integration between the two domains.

sponse to this, there has been growing interest in single-image super-resolution (SISR) reconstruction [8], which aims to recover a high-resolution (HR) IR image from its low-resolution (LR) counterpart.

In contrast to visible light images, SR tasks for IR images face the challenge of limited sample availability. This scarcity is primarily attributed to the high cost of IR cameras, which necessitate larger-aperture optical components and more sensitive sensors [6, 10, 11]. As a result, researchers often struggle to acquire a sufficient number of training samples for model development. In response, a new paradigm has emerged in IR image super-resolution, namely domain adaptation or transfer learning, where visible light images are utilized to enhance the details of IR images during the fine-tuning phase [7, 12, 13]. Visible light images, being more readily available and rich in textural de-

*This work was supported by JSPS KAKENHI Grant (JP23KJ0118).

tails, as visualized in Fig. 1 through FFT-transformed frequency representations, provide valuable pattern information that can significantly improve the quality of IR images. Two distinct training adaptation paradigms are observed: the Hybrid and the Decoupled models. 1) The Hybrid approach employs visible samples during the pre-training phase to offset the scarcity of IR samples, albeit at the cost of entangled feature spaces for both image types [12, 13]. 2) The Decoupled model by Huang *et al.* [7] leverages a dual-branch architecture for independent feature extraction from visible and IR samples, achieving pattern decoupling in the feature space. Nonetheless, the approach fails to differentiate between positive texture and negative noise features. As illustrated in Fig. 1, a previous approach to feature domain adaptation can inadvertently transfer these degradation features from the visible light domain to the IR domain, further compromising the quality of the SR images.

Considering the aforementioned analyses, we introduce a novel training framework, *Target-oriented Domain Adaptation SRGAN (DASRGAN)*, specifically crafted for SR tasks in IR imaging. This framework is strategically designed to selectively incorporate beneficial features, such as texture details, while effectively suppressing detrimental ones, including noise. Specifically, our work adopts a dual-faceted approach to tackle both noise and texture features. We introduce a noiseless adversarial loss that generates Gaussian noise patterns, frequently encountered in SR tasks [7, 14, 15], to diverge the generative and noise pattern distributions. This guides the generator to minimize focus on noise-related features. Concurrently, we enhance feature extraction capabilities with a specialized discriminator that incorporates a Sobel-prior extraction branch. This Sobel-based module excels in texture detection [16, 17] and is employed alongside Sobel-guided priority adversarial loss to optimize the alignment of texture-related prior distributions.

In summary, our primary contributions are threefold and centered around the introduction of DASRGAN, a framework architected for SR tasks in IR imaging. This framework is characterized by its bifocal adaptation mechanism aimed at both enhancing texture fidelity and mitigating noise. 1) *Texture-Oriented Adaptation (TOA)*: We introduce a specialized discriminator, $\mathbb{D}_{s_{\text{trans}}}$, equipped with a Sobel-prior extraction branch, sharpens focus on texture details during adversarial training. Additionally, we propose a novel Texture-Oriented Prior Adversarial Loss, $\mathcal{L}_{\text{trans}}$, formulated to guide the generator network \mathbb{G} in the meticulous alignment of texture patterns. 2) *Noise-Oriented Adaptation (NOA)*: We unveil a new Noise-Oriented Adversarial Loss, $\mathcal{L}_n^{\mathbb{G}}$, explicitly engineered to direct the generator network in attenuating the transference of noise between the visible and IR spectral domains. 3) Our experiments show that DASRGAN significantly surpasses existing methods, setting a new standard in IR image SR tasks both qualita-

tively and quantitatively.

2. Related Works

2.1. Deep Networks for IR Image SR

With the advent of deep learning, neural networks have shown extraordinary capabilities in SR tasks, leading to increased interest in their application for IR image enhancement [18–21]. A key focus in IR image super-resolution is the reconstruction of edge details, which are inherently more challenging to capture in IR images compared to visible light images [20, 22]. This challenge stems from the unique physical models [23] that govern thermal radiation detection in IR imaging and the synthesis of IR images [24, 25]. In IR images, high-frequency and low-frequency information typically represent image outlines and edges, respectively. However, the edge information in IR images is generally sparser than in visible light images, rendering the task more challenging.

The challenge of utilizing deep learning to restore intricate details in IR images through non-explicit models is garnering increasing interest. On one hand, Marivani *et al.* [18] initially proposed the integration of sparse edge information from visible light images, along with the fusion of interpretable sparse priors, to aid in IR image reconstruction. Experimental results indicate that enhanced neural networks employing multiple receptive fields contribute to performance improvement [19, 26]. On the other hand, researchers have explored the rich detail present in visible light images to improve IR image quality. This is achieved by designing modules for high-frequency information extraction from visible light images and employing attention mechanisms to judiciously introduce pattern information into the IR feature domain [7, 19, 27, 28]. While these methods typically follow a pre-train and fine-tune paradigm, they risk transferring undesirable features like noise from the visible light domain. Our study counters this by introducing target-oriented deep learning frameworks, specifically designed to overcome these limitations and enhance IR images.

2.2. Target-oriented Domain Adaptation

To enhance the restoration of intricate textures in SR tasks IR images, there is a growing trend to incorporate pattern information from visible light images. This approach has prompted an exploration into the domain adaptation challenges between visible and IR feature domains. Typically, domain adaptation involves transferring knowledge from one or several source domains $\mathcal{S}_1, \dots, \mathcal{S}_i$ to train a model that effectively generalizes to a different yet related target domain \mathcal{T} [29–31]. In IR image SR, visible light images constitute the source domain, with the IR feature domain being the target.

Previous research [32–35] has shown that domain adaptation strategies can affect final performance due to the inclusion of irrelevant features from the source domain. Thus, it’s crucial to explicitly decompose source domain features into task-relevant components, allowing the model to concentrate on pertinent priors [35, 36]. In this study, we introduce a dual-faceted framework aimed at facilitating feature domain alignment. Specifically, we propose texture-oriented and noise-oriented strategies. The texture-oriented approach focuses on aligning relevant texture information between the source and target domains, while the noise-oriented strategy works to reduce the transfer of undesirable noise features. This comprehensive approach aims to tackle the complexities associated with domain adaptation for IR image SR tasks.

3. Methodology

In the realm of SISR for IR imagery, traditional techniques [14] often rely on paired training data denoted by $\{x_{ir}, y_{ir}\}$. Here, $x_{ir} \in \mathbb{R}^{\frac{H}{\mu} \times \frac{W}{\mu} \times 1}$ and $y_{ir} \in \mathbb{R}^{H \times W \times 1}$ correspond to low- and high-resolution IR images, respectively, where μ signifies the spatial upscaling factor affecting both dimensions, height (H) and width (W). Conversely, state-of-the-art approaches [7, 12, 13] utilize a visible light counterpart, $x_{vis} \in \mathbb{R}^{\frac{H}{\mu} \times \frac{W}{\mu} \times C}$, in a triplet formation $\{x_{ir}, x_{vis}, y_{ir}\}$ to augment the super-resolution reconstruction of IR images. Here, C signifies the RGB image’s channel count, usually three.

We now introduce the notational conventions and specialized formulations incorporated in the DASRGAN framework, engineered to tackle the SISR challenge, which is intrinsically an ill-posed problem [14]. The analysis begins with the consideration of IR-visible pairs $\{x_{ir}, y_{ir}\}$, with x denoting the LR and y the HR samples. In terms of domain adaptation, the dataset is designated as $S_{vis} := \{(x_{vis}, y_{ir})\}_{i=1}^N$, where x_{vis} originating from the visible light LR distribution $\mathcal{D}_{x_{vis}}$. Furthermore, we construct a parametric model predicated on the source dataset $S_{ir} := \{(x_{ir}, y_{ir})\}_{i=1}^N$, x_{ir} sampled from IR-LR distribution $\mathcal{D}_{x_{ir}}$. Note that the deployed model operates in a distinct test or target distribution, $\mathcal{D}_{x_{ir}}$, potentially diverging significantly from the source distribution, $\mathcal{D}_{x_{vis}}$. This variation necessitates robust domain adaptation techniques, which are addressed by the target-centric DASRGAN methodology.

The subsequent subsections outline DASRGAN’s two-stage alternating training paradigm. Sec. 3.2 details the network architecture, while Sec. 3.3 and Sec. 3.4 elaborate on TOA and NOA, respectively.

3.1. Training paradigm of DASRGAN

Our target-oriented DASRGAN training incorporates two round-based stages alternating of IR and visible light

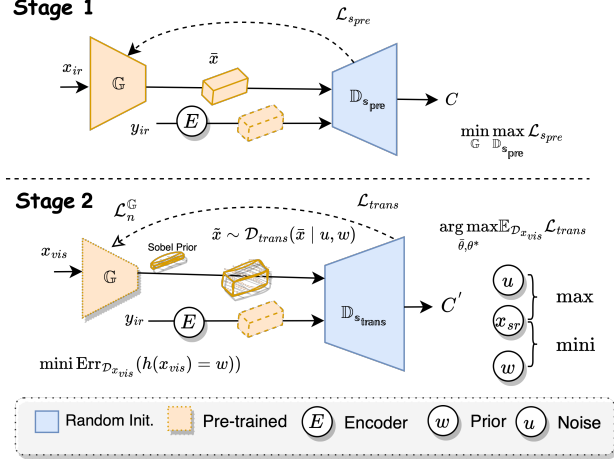


Figure 2. During training, DASRGAN employs an alternating input strategy, feeding the model with LR-HR pairs of $\{x_{ir}, y_{ir}\}$ and $\{x_{vis}, y_{ir}\}$ in each iteration.

domains. A comprehensive overview of our approach is illustrated in Fig. 2.

Stage 1. The low resolution IR image x_{ir} is fed to the generator network \mathbb{G} to invert the input into a latent vector \tilde{x} . Then the \tilde{x} and the paired high-resolution IR image y_{ir} are fed to the discriminator network \mathbb{D}_{spre} to output a scalar C . The objective function is denoted as

$$\min_{\mathbb{G}} \mathcal{L}_{MAE}(x_{ir}, y_{ir}); \min_{\mathbb{D}_{spre}} \mathcal{L}_{spre}(x_{ir}, y_{ir}) \quad (1)$$

where the pre-training function \mathcal{L}_{spre} is the cross-entropy loss, which aims to maximize the likelihood data distribution $\mathcal{D}_{x_{ir}}$ of the paired samples in S_{ir} . \mathbb{D}_{spre} is trained to minimize \mathcal{L}_{spre} in an adversarial manner. Note that \mathbb{G} is also trained to minimize the MAE loss.

Stage 2. Visible light LR images x_{vis} are fed into a pre-trained \mathbb{G} encoded to output latent vectors $\tilde{x} \sim \mathcal{D}_{trans}(\tilde{x} | u, w)$. The paired data, x_{vis} and y_{ir} , are fed to the discriminator network \mathbb{D}_{strans} output scalar C' . \mathcal{D}_{trans} is defined as the conditional probability distribution, i.e., the conditional probability to sample \tilde{x} under the prior w and noise u conditions. Denote \mathcal{H} as the hypothesis sets. We define the error of network $h \in \mathcal{H}$ on \mathcal{D}_{trans} as:

$$\epsilon_{\mathcal{D}_{trans}}(h) = \mathbb{E}_{(x_{vis}, y_{ir}) \sim \mathcal{D}_{x_{vis}}} [\ell(h(x_{vis}), y_{ir})] \quad (2)$$

For $\ell(h(x_{vis}), y_{ir})$, where ℓ is the usual indicator function, we use $\mathcal{L}^{\mathbb{G}}$ to denote it is the ℓ . Details will be discussed in Sec. 4. In the domain adaptation phase, we seek to minimize the risk of error $\min \text{Err}_{\mathcal{D}_{x_{vis}}}$, by bridging the distance between w and \tilde{x} . When the network converges, \mathbb{G} represents a nonlinear mapping between x_{vis} and w . The formalization is as follows:

$$\min \text{Err}_{\mathcal{D}_{x_{vis}}}(h(x_{vis}) = w) \quad (3)$$

On the other hand, we seek to learn the optimal parameters $\theta_{\mathbb{D}_{strans}}$ of the \mathbb{D}_{strans} by maximizing the expected risk, θ

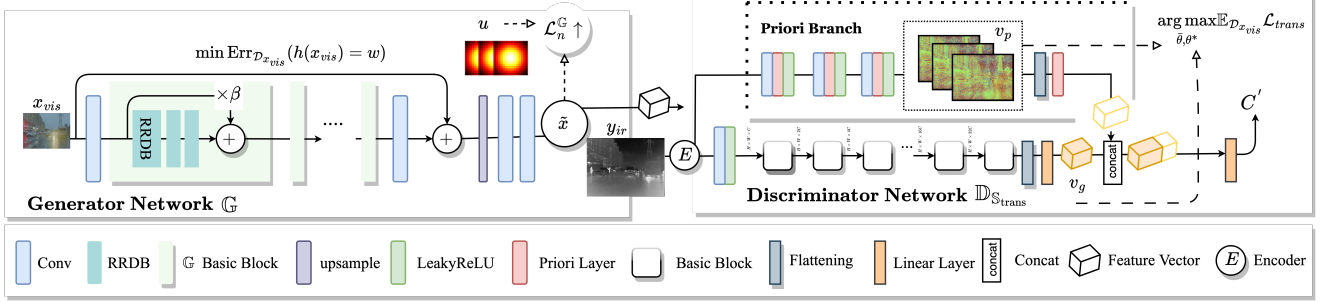


Figure 3. **Illustration of adversarial learning Stage 2: Target-Oriented Domain Adaptation.** (1) For the pre-trained \mathbb{G} , the visible images x_{vis} are fed and then encoded into \tilde{x} . The blur kernel latent scores are randomly generated and denoted as u . The loss function \mathcal{L}_n^G is designed to evaluate the difference between the degradation information in u and \tilde{x} , and to minimize u through optimization. (2) For \mathbb{D}_{strans} , novel priori branch is proposed. \tilde{x} is encoded by the priori branch and outputs a latent vector v_p , which includes information about the details of the visible domain, *e.g.*, edges. After the concat with the main path output v_g , v_p converted to new feature vectors and mapped to a scalar C' . The objective function is denoted as \mathcal{L}_{trans} .

and θ^* denote the parameters from the stage 1 initialization and the parameters being updated, respectively:

$$\theta_{\mathbb{D}_{strans}} = \arg \max_{\theta, \theta^*} \mathbb{E}_{\mathcal{D}_{x_{vis}}} \mathcal{L}_{trans}(x_{vis}, y_{ir}) \quad (4)$$

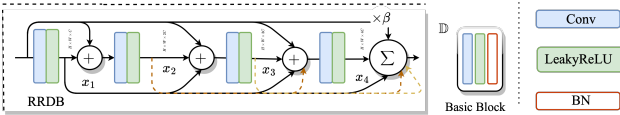


Figure 4. The Architecture of Residual in Residual Dense Block (RRDB) and Basic Block.

3.2. Network Architecture

In this study, our primary objective is not to develop complex generator architectures for enhanced performance in infrared (IR) super-resolution tasks. Instead, we introduce a novel discriminator, \mathbb{D}_{strans} , during the domain adaptation phase. This discriminator is specifically designed to facilitate target-oriented domain adaptation, with a special emphasis on enhancing texture details. An illustration of this adversarial training stage can be found in Fig. 3.

For the generator \mathbb{G} , we utilize the architecture from previous studies [37, 38], incorporating the Residual-in-Residual Dense Block (RRDB) as the core module. The RRDB, featuring skip connections and up-sampling layers, is depicted in Fig. 4. Its proven effectiveness in Gaussian-based and blind SR tasks [38] demonstrates its capacity to aptly fit super-resolution dataset distributions.

Regarding the discriminator, we present a novel \mathbb{D}_{strans} , specifically crafted for the domain adaptation phase. This design includes an a priori branch \mathcal{B} , engineered to encode the detailed texture of x_{vis} into an a priori latent variable v_p . Employing the Sobel operator [39] as

the a priori layer, it excels in capturing texture detail patterns, given the Sobel operator’s notable efficiency in edge detection [39, 40] and detail texturing. Our ablation studies suggest that extracting mid-level textures is most effective, which will be discussed further in Sec. 4. The architecture of \mathbb{D}_{strans} can be mathematically formalized as follows:

$$C' = L(\text{concat}(\mathcal{B}(x_{vis}), \mathcal{M}(x_{vis}))) \quad (5)$$

where \mathcal{M} serves as the primary feature extraction branch. After encoding, latent variables are concatenated and fed into a linear layer L for feature mapping. C' is the scalar output produced by the discriminator. Details on the texture-oriented and noise-oriented domain adaptation losses, integral to our framework, will be elaborated in Sec. 3.3 and Sec. 3.4, respectively.”.

3.3. Texture-Oriented Adaptation

For TOA, our objective is to reconcile the distributional disparities between visible and IR images with respect to texture priors. \mathbb{D}_{strans} is designed to guide the generator \mathbb{G} in synthesizing realistic texture priors. This is achieved by maximizing the expected risk Err through adversarial training [31], formulated as follows:

$$\begin{aligned} \text{Err}[\mathcal{D}_{x_{ir}}, \theta, \ell(x_{ir}, y_{ir}, \theta)] &= \mathbb{E}_{(x_{ir}, y_{ir}) \sim \mathcal{D}_{x_{ir}}} [\ell(x_{ir}, y_{ir}, \theta)] \\ &= \mathbb{E}_{(x_{vis}, y_{ir}) \sim \mathcal{D}_{x_{vis}}} \left[\frac{\mathcal{D}_{x_{ir}}}{\mathcal{D}_{x_{vis}}} \ell \right] \quad (6) \\ &= \mathbb{E}_{(x_{vis}, y_{ir}) \sim \mathcal{D}_{x_{vis}}} [\beta \ell] \end{aligned}$$

Here, $\mathcal{D}_{x_{vis}}$ and $\mathcal{D}_{x_{ir}}$ denote the probability distributions of S_{vis} and S_{ir} , respectively. ℓ represents the loss function, and $\beta(x_{vis}, x_{ir})$ is the ratio between the two probability distributions, effectively serving as a weighting coefficient. Notably, when $\mathcal{D}_{x_{vis}} = \mathcal{D}_{x_{ir}}$, β simplifies to 1. Given that the dense estimate β remains constant, the texture-oriented loss function ℓ is expected to enhance the performance of

domain adaptation. In our work, we introduce the prior adversarial loss $\mathcal{L}_{\text{trans}}$ as ℓ to evaluate the quality of predicted images in prior-detection. Specifically, we employ the Sobel operator to extract edge features from both the predicted and ground-truth images I . The Sobel features, denoted as \mathcal{S}_P and \mathcal{S}_T for the predicted and target images respectively, are computed using the formula:

$$\mathcal{S} = \sqrt{(G_h \odot I)^2 + (G_v \odot I)^2} \quad (7)$$

where G_h and G_v are the Sobel kernels for horizontal and vertical edge detection, and \odot represents the convolution operation. The $\mathcal{L}_{\text{trans}}$ between these Sobel features is then calculated and normalized by the total number of pixels N :

$$\mathcal{L}_{\text{trans}} = \frac{1}{N} \sum_{i,j} |\mathcal{S}_P(i,j) - \mathcal{S}_T(i,j)| \quad (8)$$

3.4. Noise-Oriented Adaptation

For NOA, our approach aims to address the issue of blurring degradation when transferring features from the visible light domain to the IR domain. To achieve this, we incorporate a noise adversarial loss function $\mathcal{L}_n^{\mathbb{G}}$ designed to quantify the perceptual divergence between \tilde{x} and an artificially generated noise pattern from u . Specifically, we utilize a pre-trained VGG [41] network to extract hierarchical features, denoted as $f_k(\tilde{x})$ and $f_k(u)$, from both the predicted image and the noise pattern at the k^{th} layer. The loss at each layer k is calculated as the negative L_1 distance between these feature vectors, scaled by a layer-specific weight w_k . Formally, the $\mathcal{L}_n^{\mathbb{G}}$ is defined as:

$$\mathcal{L}_n^{\mathbb{G}}(\tilde{x}, u) = - \sum_k w_k \times \|f_k(\tilde{x}) - f_k(u)\|_1 \quad (9)$$

The overall loss function is a weighted aggregation of this noise adversarial loss function, with the weight empirically set to 1.0 in our experiments. This specialized loss function serves to guide the network towards generating images that are perceptually different to natural noise patterns, thereby enhancing the model’s adaptation ability. This is particularly advantageous in scenarios involving Gaussian blurred scenes, a common occurrence in the visible feature domain. The objective function of DASRGAN at stage 2 is

$$\min_{\mathbb{G}} \max_{\mathbb{D}_{\text{strans}}} V(\mathbb{D}_{\text{strans}}, \mathbb{G}) = E_{y_{ir}} [\log \mathbb{D}_{\text{strans}}(y_{ir})] + E_{x_{vis}} [\log(1 - \mathbb{D}_{\text{strans}}(\mathbb{G}(x_{vis})))] \quad (10)$$

where $\log \mathbb{D}_{\text{strans}}(y_{ir})$ is the cross-entropy between $[1, 0]^T$ and $[\mathbb{D}_{\text{strans}}(y_{ir}), 1 - \mathbb{D}_{\text{strans}}(y_{ir})]^T$. Similarly, $\log(1 - \mathbb{D}_{\text{strans}}(\mathbb{G}(x_{vis})))$ is the cross-entropy between $[1, 0]^T$ and $[\mathbb{D}_{\text{strans}}(\mathbb{G}(x_{vis})), 1 - \mathbb{D}_{\text{strans}}(\mathbb{G}(x_{vis}))]^T$.

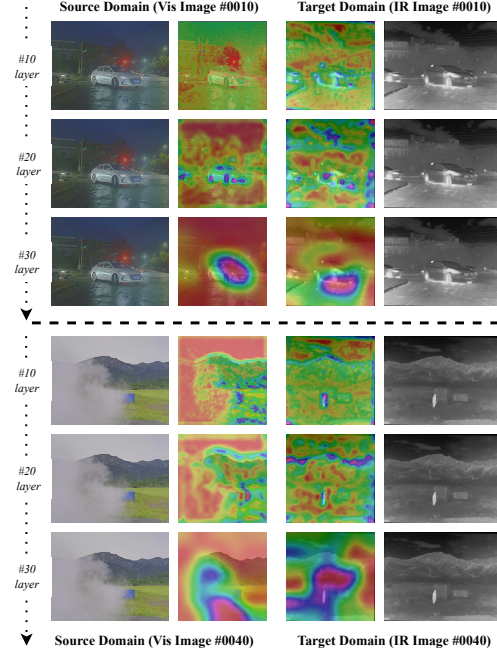


Figure 5. In each group, column 1: visible image; column 2: the feature map of the selected layer (Vis Image); column 3: the feature map of the selected layer (IR Image); column 4: IR Image.

4. Experiments

4.1. Experimental Setup

Datasets. In the training phase, we curated a paired dataset derived from Liu *et al.* [42]: M3FD Dataset, encompassing both IR and visible images. This dataset consists of 265 paired samples that include a diverse range of street-level targets such as People, Cars, Buses, among others, to rigorously assess the model’s real-world applicability. For evaluation, we created three specialized datasets: M3FD5, M3FD15, and M3FD20, from the M3FD dataset, each with different sample sizes and scene compositions. Additionally, to examine the model’s generalization performance, we compiled two more test datasets, CVC5 and CVC15, from the CVC dataset [43]. **Metrics.** Consistent with prior research, both the training and test datasets were generated using bicubic downsampling to produce LR paired samples. The evaluation phase involved assessing the generated samples using key performance metrics such as Peak Signal-to-Noise Ratio (PSNR), Mean Squared Error (MSE), and Structural Similarity Index Measure (SSIM).

Implementation details. In each minimal training batch, randomly cropped 64×64 LR images were used as input and optimized using Adam [44]. The learning rate was set to $1e-5$. Experiments were developed in PyTorch framework on an Nvidia A6000 GPU, based on basicSR [45].

Loss function. For discriminator loss $\mathcal{L}^{\mathbb{D}}$, cross-entropy

Table 1. Quantitative comparison (PSNR↑ MSE↓ SSIM↑). For Single image super-resolution on M3FD datasets. Best and second-best performances are marked in **bold** and underlined, respectively. The bottom method marked in gray adopts our model.

Scale	Methods	#Params	M3FD5			M3FD15			M3FD20		
			PSNR↑	MSE↓	SSIM↑	PSNR↑	MSE↓	SSIM↑	PSNR↑	MSE↓	SSIM↑
×2	EDSR/ <i>CVPRW 2017</i> [46]	1,369K	46.8033	1.8877	0.9903	47.5681	1.1512	0.9906	47.6258	0.9873	0.9915
	ESRGAN/ <i>ECCVW 2018</i> [37]	16,661K	47.7307	1.3792	0.9920	48.0642	1.0141	0.9910	48.0353	0.8923	0.9918
	FSRCNN/ <i>ECCV 2016</i> [47]	475K	45.4145	2.5077	0.9892	45.3984	1.8363	0.9901	46.0699	1.4521	0.9911
	SRGAN/ <i>CVPR 2017</i> [48]	1,369K	46.7851	1.8836	0.9903	47.7077	1.1141	0.9906	47.5877	0.9867	0.9915
	SwinIR/ <i>ICCV 2021</i> [49]	11,752K	46.7244	1.8973	0.9902	47.1768	1.2517	0.9901	47.4024	1.0424	0.9912
	SRCNN/ <i>T-PAMI 2015</i> [50]	57K	45.2227	2.6043	0.9889	45.2058	1.9163	0.9899	46.0374	1.4761	0.9910
	RCAN/ <i>ECCV 2018</i> [15]	12,467K	46.8454	1.7348	0.9911	47.5058	1.1610	0.9909	47.5261	1.0085	0.9918
	PSRGAN/ <i>SPL 2021</i> [7]	2,414K	46.3526	2.2219	0.9895	47.3337	1.2204	0.9903	47.2350	1.0842	0.9912
	Shuffle (base)/ <i>NIPS'22</i> [51]	393K	47.2429	1.5639	0.9913	47.7097	1.1100	0.9907	47.7688	0.9554	0.9915
	Shuffle (tiny)/ <i>NIPS'22</i> [51]	108K	46.7761	1.8953	0.9902	47.5158	1.1563	0.9906	47.5547	0.9959	0.9914
	SAFMN/ <i>ICCV 2023</i> [9]	5,559K	48.0102	1.0881	0.9917	48.3006	0.8202	0.9909	48.4714	0.6981	0.9917
	HAT <i>CVPR 2023</i> [52]	20,624K	48.3822	0.9813	0.9923	48.4636	0.7720	0.9914	48.7168	0.6545	0.9920
Ours	16,661K	48.3865	<u>0.9982</u>	<u>0.9922</u>	48.8402	0.7148	0.9915	48.7952	0.6410	<u>0.9919</u>	
×4	EDSR/ <i>CVPRW 2017</i> [46]	1,517K	39.1096	13.6760	0.9523	40.6962	5.4159	0.9712	40.9810	4.8430	0.9742
	ESRGAN/ <i>ECCVW 2018</i> [37]	16,697K	40.2261	9.3695	0.9544	41.8889	3.5478	0.9720	42.1464	3.1274	0.9751
	FSRCNN/ <i>ECCV 2016</i> [47]	623K	39.1111	10.8185	0.9509	40.1994	5.1549	0.9703	40.9195	4.2574	0.9734
	SRGAN/ <i>CVPR 2017</i> [48]	1,517K	40.0669	9.7075	0.9531	41.8255	3.5842	0.9717	42.0157	3.2603	0.9745
	SwinIR/ <i>ICCV 2021</i> [49]	11,900K	39.1953	10.6050	0.9520	40.4065	4.8949	0.9710	40.9260	4.1474	0.9741
	SRCNN/ <i>T-PAMI 2015</i> [50]	168K	37.2484	14.2045	0.9400	37.7955	9.2622	0.9601	39.0011	6.9846	0.9652
	RCAN/ <i>ECCV 2018</i> [15]	12,614K	39.3303	10.7535	0.9519	40.3756	4.9195	0.9713	41.1036	4.1006	0.9746
	PSRGAN/ <i>SPL 2021</i> [7]	2,414K	39.4035	10.3635	0.9518	40.7592	4.4829	0.9709	41.3344	3.7767	0.9738
	Shuffle (base)/ <i>NIPS'22</i> [51]	410K	40.1626	9.0440	0.9553	41.5322	3.8124	0.9714	41.8758	3.4093	0.9747
	Shuffle (tiny)/ <i>NIPS'22</i> [51]	112K	39.7708	9.9019	0.9530	41.2227	4.0582	0.9714	41.6794	3.5265	0.9743
	HAT <i>CVPR 2023</i> [52]	20,772K	39.8073	9.8251	0.9527	41.2769	4.0311	0.9709	41.7172	3.4732	0.9742
	SAFMN/ <i>ICCV 2023</i> [9]	5,600K	40.5748	7.2981	0.9604	41.3232	4.0054	0.9713	41.9802	3.3822	0.9748
Ours	16,697K	40.5088	<u>8.7855</u>	<u>0.9558</u>	42.1196	3.3763	0.9724	42.3179	3.0009	0.9755	

loss and prior adversarial loss $\mathcal{L}_{\text{trans}}$ are used. Discriminator maximizes the difference between real and predicted distributions, using a negative loss setting to minimize the loss function and optimize parameters. For the generator loss \mathcal{L}^G , MAE and noise adversarial losses \mathcal{L}_n^G are used. α and β are the balancing weights:

$$\begin{aligned} \mathcal{L}^G &= \mathcal{L}_{MAE} + \alpha \mathcal{L}_n^G \\ \mathcal{L}^D &= -(\mathcal{L}_{\text{spre}} + \beta \mathcal{L}_{\text{trans}}) \end{aligned} \quad (11)$$

Table 2. Quantitative comparison (PSNR↑ MSE↓ SSIM↑). For IR image super-resolution on CVC datasets. Best and second-best performances are marked in **bold** and underlined, respectively. The bottom method marked in gray adopts our model.

Scale	Methods	CVC15			CVC5		
		PSNR↑	MSE↓	SSIM↑	PSNR↑	MSE↓	SSIM↑
×2	Shuffle (base)/ <i>NIPS'22</i> [51]	42.0601	4.7414	0.9634	41.7926	4.5484	0.9696
	Shuffle (tiny)/ <i>NIPS'22</i> [51]	42.1647	4.6198	0.9640	41.9064	4.4140	0.9701
	HAT <i>CVPR 2023</i> [52]	42.7350	<u>3.4555</u>	0.9633	42.5018	<u>3.2517</u>	0.9697
	SAFMN/ <i>ICCV 2023</i> [9]	35.7437	-	0.9523	34.9967	-	0.9583
	Ours	42.7978	3.4066	<u>0.9638</u>	42.5404	3.2298	<u>0.9700</u>
×4	Shuffle (base)/ <i>NIPS'22</i> [51]	38.7197	8.1912	0.9357	38.5379	8.2922	0.9439
	Shuffle (tiny)/ <i>NIPS'22</i> [51]	38.7721	8.0796	<u>0.9358</u>	38.5120	8.3231	0.9438
	HAT <i>CVPR 2023</i> [52]	38.7845	<u>8.0508</u>	0.9358	38.5250	8.3395	0.9437
	SAFMN/ <i>ICCV 2023</i> [9]	29.9648	-	0.9113	28.2868	-	0.9196
	Ours	38.9397	7.7844	0.9378	38.7182	7.9386	0.9462

4.2. Quantitative Results

Tab. 1 provides a comprehensive quantitative comparison of various SISR methods on the M3FD datasets. The evaluation metrics include PSNR, MSE, and SSIM. The evaluation of various methods is conducted across multiple scales (×2 and ×4) and distinct versions of the M3FD dataset (M3FD5, M3FD15, M3FD20). Additionally, the number of parameters for each model is disclosed, offering a lens into the complexity of the respective models. Remarkably, our proposed method (highlighted in gray) consistently outshines other state-of-the-art techniques across nearly all performance metrics and dataset versions. It registers the highest PSNR and SSIM scores while simultaneously achieving the lowest MSE, thereby signifying exceptional image quality and structural integrity. In terms of parameter efficiency, our model demonstrates superior performance despite having a parameter count comparable to that of ESRGAN [37], thus indicating optimized parameter utilization. Contemporary methods such as HAT [52] and SAFMN [9] exhibit competitive performance but ultimately fall short of the benchmarks set by our method. Legacy algorithms like SRCNN [50] and FSRCNN [47] lag in performance metrics, underscoring the DASRGAN advancements

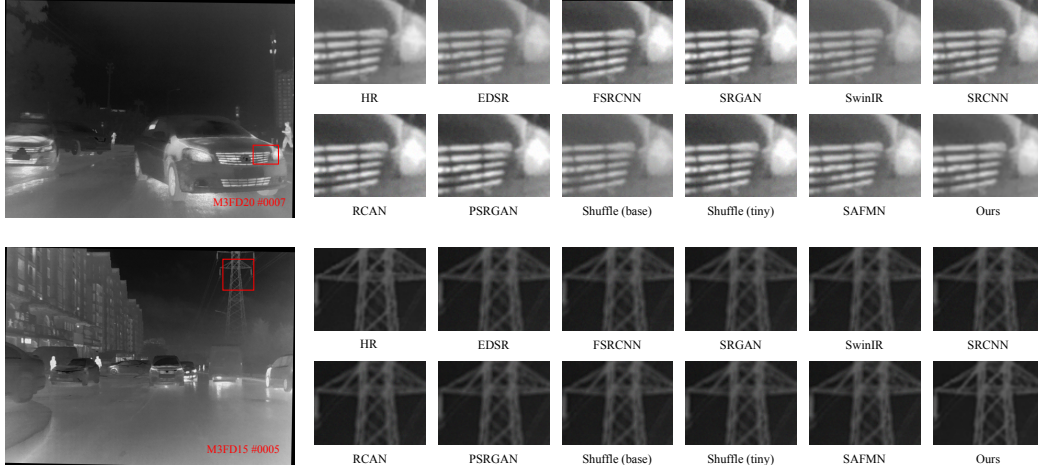


Figure 6. Visual comparison of $\times 2$ image super-resolution methods (M3FD Datasets). Zoom-in for better details.

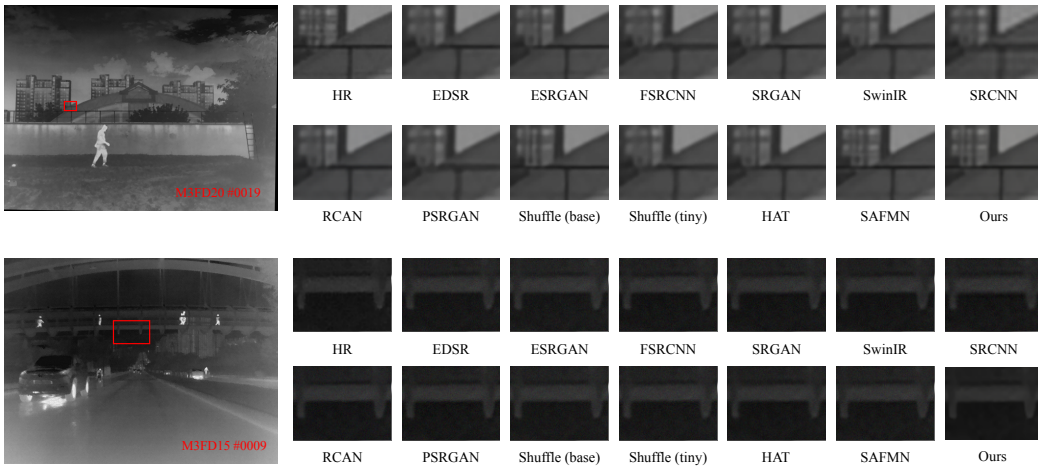


Figure 7. Visual comparison of $\times 4$ image super-resolution methods (M3FD Datasets). Zoom-in for better details.

in the field of IR image super-resolution. Importantly, our model sustains a consistent lead across different scales, reinforcing its robustness and scalability.

To rigorously assess DASRGAN’s robustness, we conducted tests on the CVC dataset (see Tab. 2). Our model consistently outperforms benchmarks across all scales on both CVC15 and CVC5 datasets, achieving the highest PSNR, the lowest MSE, and top-ranking SSIM. This establishes its state-of-the-art status. In terms of scale robustness, our model sustains its superior performance across varying scales ($\times 2$ & $\times 4$), reinforcing its adaptability. While HAT [52] and Shuffle (tiny) [51] show competitive results, they are outperformed by our approach. Conversely, SAFMN [9] lags significantly, indicating limited robustness across diverse IR feature domains. Our model excels across all key metrics, underscoring its comprehensive effectiveness for IR image super-resolution tasks.

Table 3. Ablation studies of domain adaptation. Quantitative results of PSNR without visible light domain adaptation and adaptation results with pretraining are shown separately (**w/o & w**).

Dataset	PSRGAN [7] $\times 2$	SRGAN [48] $\times 2$	ESRGAN [37] $\times 2$	Ours $\times 2$
M3FD15	47.02/46.87	45.21/46.12	45.77/45.86	47.02/48.84 [1.82dB \uparrow]
M3FD20	46.55/45.02	45.56/46.50	46.17/46.36	47.21/48.79 [1.58dB \uparrow]

Table 4. Structural ablation study. From left to right, modules are added, and upsampling factors for $\times 2$ & $\times 4$ are shown ($\times 2 \mid \times 4$).

Dataset	Metrics \uparrow	Pre train \rightarrow	+ $\mathbb{D}_{s_{trans}}$ \rightarrow	+ \mathcal{L}_n^G \rightarrow	+ \mathcal{L}_{trans}
M3FD15	PSNR	47.02/40.11	48.10/41.63	48.20/41.63	48.84/42.11
	SSIM	0.9900/0.8682	0.9903/0.9723	0.9913/0.9723	0.9915/0.9724
M3FD20	PSNR	47.21/40.83	47.42/41.77	48.06/41.77	48.79/42.31
	SSIM	0.9909/0.9744	0.9912/0.9754	0.9920/0.9755	0.9919/0.9755

4.3. Ablation Study

Effectiveness of the domain adaptation. The domain adaptation strategy is beneficial to the PSNR metrics. How-

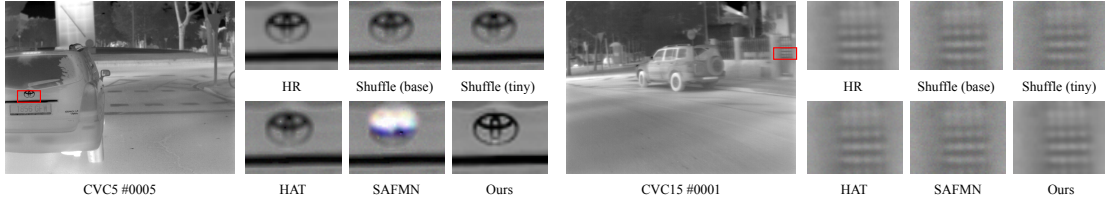


Figure 8. Visual comparison of $\times 2$ image super-resolution methods (CVC Datasets). Zoom-in for better details.

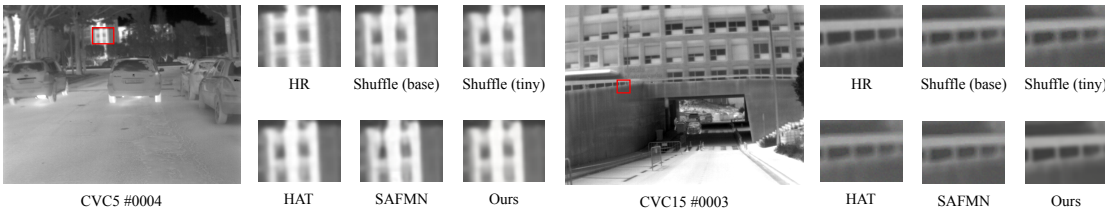


Figure 9. Visual comparison of $\times 4$ image super-resolution methods (CVC Datasets). Zoom-in for better details.

Table 5. Prior ablation studies. From left to right: shallow, middle, and deep priors were selected separately (PSNR/SSIM).

Dataset	Shallow Prior		Middle Prior		Deep Prior	
	$\times 2$	$\times 4$	$\times 2$	$\times 4$	$\times 2$	$\times 4$
M3FD15	47.21/0.9863	41.23/0.9622	48.01/0.9889	41.66/0.9712	47.33/0.9871	41.36/0.9672
M3FD20	46.92/0.9811	41.11/0.9598	47.32/0.9901	41.53/0.9688	47.32/0.9901	41.13/0.9602

ever, the performance of PSRGAN [7], a model sensitive to negative features (e.g., noise), declines if the feature domains are directly transferred. DASRGAN’s target-oriented domain adaptation strategy achieves better performance than its competitors (see Tab. 3). **Effectiveness of Target-oriented.** To rigorously assess the efficacy of the proposed DASRGAN model, we conducted a series of preliminary experiments. The results show consistent gains with the stepwise addition of $\mathbb{D}_{s_{\text{trans}}} \rightarrow +\mathcal{L}_n^G \rightarrow +\mathcal{L}_{\text{trans}}$. This confirms the utility of both a priori and noise-based domain adaptation in SR tasks for IR images. For detailed metrics, see Tab. 4. **Effectiveness of Prior.** To evaluate the impact of texture priors across feature layers, we compare results in Tab. 5. The data shows that introducing texture prior at the middle layer is most effective for enhancing IR image details. Deep priors focus on high-level semantics, making them ideal for object detection, while mid priors better capture background texture, optimizing detail recovery in IR images (see Fig. 5). **Hyper-parameter Ablation** In the hyperparameter ablation study, the optimal setting is found to be $\alpha = 0.1$ and $\beta = 1.0$, yielding the highest performance across all metrics. Conversely, a configuration with $\alpha = 1.0$ and $\beta = 0.0$ results in the poorest performance. The model demonstrates greater sensitivity to β than α (see Tab. 6).

Table 6. Hyperparameter ablation study $\times 2$, where α is the weight of \mathcal{L}_n^G and β is the weight of $\mathcal{L}_{\text{trans}}$.

α / β	M3FD5	M3FD15	M3FD20
0.1/0.0	48.32/0.9922	48.75/0.9914	48.71/0.9919
0.0/1.0	48.84/0.9915	48.84/0.9900	48.79/0.9918
0.5/1.0	44.19/0.9920	44.65/0.9914	45.06/0.9919
0.5/0.1	47.93/0.9923	48.17/0.9913	48.15/0.9920
1.0/0.0	39.99/0.9504	41.63/0.9723	41.77/0.9755
0.1/1.0	48.38/0.9922	48.84/0.9915	48.79/0.9919

4.4. Visual Comparison

In Fig. 6 & Fig. 7, we present a visual comparison featuring images "0007" "0005" "0009" "0019" from the M3FD15 & M3FD20 dataset. DASRGAN effectively recovers crisp lattice structures, whereas competing methods exhibit pronounced blurring. Similar observations can be made for the "0019" image in the M3FD20 dataset, where DASRGAN excels in restoring clear textures for the characters. These visual outcomes further underscore the superior performance of our approach. In our evaluation, we extend the scope to assess the SR model’s adaptability across varying data distributions. We juxtapose the performance of the benchmark method with that of DASRGAN on the CVC dataset, as illustrated in Fig. 8 and Fig. 9. Through qualitative analysis, DASRGAN consistently outperforms in blur reduction and artifact minimization. On the other hand, competing methods exhibit shortcomings such as the emergence of ringing artifacts—particularly noticeable in CVC 0003—or fail to recover texture details, resulting in lingering blur adequately.

5. Conclusion

In this study, we present a novel framework, Target-oriented Domain Adaptation SRGAN, specifically designed

for IR image super-resolution via visible image feature domain target-oriented adaptation to enhance IR image. The framework is built on two pivotal components: 1) Texture-Oriented Adaptation, which enhances texture fidelity through a specialized prior adversarial loss $\mathcal{L}_{\text{trans}}$ and a tailored discriminator $\mathbb{D}_{s_{\text{trans}}}$ to transfer the visible image textural features, and 2) Noise-Oriented Adaptation, aimed at minimizing noise transfer from feature domain via an innovative noise adversarial loss \mathcal{L}_n^G . Our comprehensive experiments confirm the effectiveness of these state-of-the-art components, establishing new benchmarks in both qualitative and quantitative assessments.

References

- [1] J. Lukose, S. Chidangil, and S. D. George, "Optical technologies for the detection of viruses like covid-19: Progress and prospects," *Biosensors & Bioelectronics*, vol. 178, pp. 113 004 – 113 004, 2021. **1**
- [2] J. Torra, F. Viela, D. Megías, B. Sot, and C. Flors, "Versatile near-infrared super-resolution imaging of amyloid fibrils with the fluorogenic probe cranad-2." *Chemistry*, 2022. **1**
- [3] J. Wu, X. Li, and Y. Zhou, "An infrared image detection of power equipment based on super-resolution reconstruction and yolov4," *The Journal of Engineering*, vol. 2022, no. 10, pp. 1006–1016, 2022. **1**
- [4] J. Nie, H. Ren, Y. Zheng, D. Ghent, and K. Tansey, "Land surface temperature and emissivity retrieval from nighttime middle-infrared and thermal-infrared sentinel-3 images," *IEEE Geoscience and Remote Sensing Letters*, vol. 18, no. 5, pp. 915–919, 2020. **1**
- [5] H. Gupta and K. Mitra, "Toward unaligned guided thermal super-resolution," *IEEE Transactions on Image Processing*, vol. 31, pp. 433–445, 2022. **1**
- [6] Y. Huang, T. Miyazaki, X. Liu, and S. Omachi, "Infrared image super-resolution: Systematic review, and future trends," *arXiv preprint arXiv:2212.12322*, 2022. **1**
- [7] Y. Huang, Z. Jiang, R. Lan, S. Zhang, and K. Pi, "Infrared image super-resolution via transfer learning and psrgan," *IEEE Signal Processing Letters*, vol. 28, pp. 982–986, 2021. **1, 2, 3, 6, 7, 8**
- [8] W. Yang, X. Zhang, Y. Tian, W. Wang, J.-H. Xue, and Q. Liao, "Deep learning for single image super-resolution: A brief review," *IEEE Transactions on Multimedia*, vol. 21, no. 12, pp. 3106–3121, 2019. **1**
- [9] L. Sun, J. Dong, J. Tang, and J. Pan, "Spatially-adaptive feature modulation for efficient image super-resolution," *arXiv preprint arXiv:2302.13800*, 2023. **1, 6, 7**
- [10] Z. He, S. Tang, J. Yang, Y. Cao, M. Y. Yang, and Y. Cao, "Cascaded deep networks with multiple receptive fields for infrared image super-resolution," *IEEE transactions on circuits and systems for video technology*, vol. 29, no. 8, pp. 2310–2322, 2018. **1**
- [11] Y. Mao, B. Zhao, D. Yan, and H. Jia, "Super-resolution reconstruction from multiple defocused infrared images of stationary scene," *IEEE Photonics Journal*, vol. 9, no. 5, pp. 1–16, 2017. **1**
- [12] T. Honda, D. Sugimura, and T. Hamamoto, "Multi-frame rgb/nir imaging for low-light color image super-resolution," *IEEE Transactions on Computational Imaging*, vol. 6, pp. 248–262, 2019. **1, 2, 3**
- [13] H. Gupta and K. Mitra, "Toward unaligned guided thermal super-resolution," *IEEE Transactions on Image Processing*, vol. 31, pp. 433–445, 2021. **1, 2, 3**
- [14] Z. Wang, J. Chen, and S. C. Hoi, "Deep learning for image super-resolution: A survey," *IEEE transactions on pattern analysis and machine intelligence*, vol. 43, no. 10, pp. 3365–3387, 2020. **2, 3**
- [15] Y. Zhang, K. Li, K. Li, L. Wang, B. Zhong, and Y. Fu, "Image super-resolution using very deep residual channel attention networks," in *Proceedings of the European conference on computer vision (ECCV)*, 2018, pp. 286–301. **2, 6**
- [16] C. Wang, B. Yu, and J. Zhou, "A learnable gradient operator for face presentation attack detection," *Pattern Recognition*, vol. 135, p. 109146, 2023. **2**
- [17] S. Dong, W. Zhou, C. Xu, and W. Yan, "Egfnnet: Edge-aware guidance fusion network for rgb–thermal urban scene parsing," *IEEE Transactions on Intelligent Transportation Systems*, 2023. **2**
- [18] I. Marivani, E. Tsiligiani, B. Cornelis, and N. Deligiannis, "Joint image super-resolution via recurrent convolutional neural networks with coupled sparse priors," in *2020 IEEE International Conference on Image Processing (ICIP)*. IEEE, 2020, pp. 868–872. **2**
- [19] Y. Yang, Q. Li, C. Yang, Y. Fu, H. Feng, Z. Xu, and Y. Chen, "Deep networks with detail enhancement for infrared image super-resolution," *IEEE Access*, vol. 8, pp. 158 690–158 701, 2020. **2**
- [20] A. Kwasniewska, J. Ruminski, M. Szankin, and M. Kaczmarek, "Super-resolved thermal imagery for high-accuracy facial areas detection and analysis," *Engineering Applications of Artificial Intelligence*, vol. 87, p. 103263, 2020. **2**
- [21] I. Marivani, E. Tsiligiani, B. Cornelis, and N. Deligiannis, "Multimodal deep unfolding for guided image super-resolution," *IEEE Transactions on Image Processing*, vol. 29, pp. 8443–8456, 2020. **2**
- [22] K. Prajapati, V. Chudasama, H. Patel, A. Sarvaiya, K. P. Upla, K. Raja, R. Ramachandra, and C. Busch, "Channel split convolutional neural network (chasnet) for thermal image super-resolution," in *Proceedings of the IEEE/CVF Conference on Computer Vision and Pattern Recognition*, 2021, pp. 4368–4377. **2**
- [23] W. Yu, Q. Peng, H. Tu, and Z. Wang, "An infrared image synthesis model based on infrared physics and heat transfer," *International journal of infrared and millimeter waves*, vol. 19, pp. 1661–1669, 1998. **2**

- [24] N. Nandhakumar, S. Karthik, and J. K. Aggarwal, "Unified modeling of non-homogeneous 3d objects for thermal and visual image synthesis," *Pattern recognition*, vol. 27, no. 10, pp. 1303–1316, 1994. [2](#)
- [25] H.-K. Hong, S.-H. Han, G.-P. Hong, and J.-S. Choi, "Simulation of reticle seekers using the generated thermal images," in *Proceedings of APCCAS'96-Asia Pacific Conference on Circuits and Systems*. IEEE, 1996, pp. 183–186. [2](#)
- [26] R. E. Rivadeneira, P. L. Suárez, A. D. Sappa, and B. X. Vintimilla, "Thermal image superresolution through deep convolutional neural network," in *Image Analysis and Recognition: 16th International Conference, ICIAR 2019, Waterloo, ON, Canada, August 27–29, 2019, Proceedings, Part II 16*. Springer, 2019, pp. 417–426. [2](#)
- [27] H. Patel, V. Chudasama, K. Prajapati, K. P. Upla, K. Raja, R. Ramachandra, and C. Busch, "Thermisrnet: an efficient thermal image super-resolution network," *Optical Engineering*, vol. 60, no. 7, pp. 073 101–073 101, 2021. [2](#)
- [28] Y. Zou, L. Zhang, Q. Chen, B. Wang, Y. Hu, and Y. Zhang, "An infrared image super-resolution imaging algorithm based on auxiliary convolution neural network," in *Optics Frontier Online 2020: Optics Imaging and Display*, vol. 11571. SPIE, 2020, pp. 335–340. [2](#)
- [29] G. Zhang, H. Zhao, Y. Yu, and P. Poupart, "Quantifying and improving transferability in domain generalization," *Advances in Neural Information Processing Systems*, vol. 34, pp. 10957–10970, 2021. [2](#)
- [30] Y. Chen, Z. Tang, K. Zhang, and Y. Liu, "Model transferability with responsive decision subjects," in *International Conference on Machine Learning*. PMLR, 2023, pp. 4921–4952. [2](#)
- [31] L. Zhang and X. Gao, "Transfer adaptation learning: A decade survey," *IEEE Transactions on Neural Networks and Learning Systems*, 2022. [2, 4](#)
- [32] S. Ben-David, J. Blitzer, K. Crammer, and F. Pereira, "Analysis of representations for domain adaptation," *Advances in neural information processing systems*, vol. 19, 2006. [3](#)
- [33] B. Sun, J. Feng, and K. Saenko, "Return of frustratingly easy domain adaptation," in *Proceedings of the AAAI conference on artificial intelligence*, vol. 30, no. 1, 2016. [3](#)
- [34] H. Tang and K. Jia, "Discriminative adversarial domain adaptation," in *Proceedings of the AAAI conference on artificial intelligence*, vol. 34, no. 04, 2020, pp. 5940–5947. [3](#)
- [35] G. Wei, C. Lan, W. Zeng, Z. Zhang, and Z. Chen, "Toalign: task-oriented alignment for unsupervised domain adaptation," *Advances in Neural Information Processing Systems*, vol. 34, pp. 13 834–13 846, 2021. [3](#)
- [36] X. Peng, Z. Huang, X. Sun, and K. Saenko, "Domain agnostic learning with disentangled representations," in *International Conference on Machine Learning*. PMLR, 2019, pp. 5102–5112. [3](#)
- [37] X. Wang, K. Yu, S. Wu, J. Gu, Y. Liu, C. Dong, Y. Qiao, and C. Change Loy, "Esrgan: Enhanced super-resolution generative adversarial networks," in *Proceedings of the European conference on computer vision (ECCV) workshops*, 2018, pp. 0–0. [4, 6, 7](#)
- [38] X. Wang, L. Xie, C. Dong, and Y. Shan, "Real-esrgan: Training real-world blind super-resolution with pure synthetic data," in *Proceedings of the IEEE/CVF international conference on computer vision*, 2021, pp. 1905–1914. [4](#)
- [39] N. Kanopoulos, N. Vasanthavada, and R. L. Baker, "Design of an image edge detection filter using the sobel operator," *IEEE Journal of solid-state circuits*, vol. 23, no. 2, pp. 358–367, 1988. [4](#)
- [40] W. Gao, X. Zhang, L. Yang, and H. Liu, "An improved sobel edge detection," in *2010 3rd International conference on computer science and information technology*, vol. 5. IEEE, 2010, pp. 67–71. [4](#)
- [41] A. Sengupta, Y. Ye, R. Wang, C. Liu, and K. Roy, "Going deeper in spiking neural networks: Vgg and residual architectures," *Frontiers in neuroscience*, vol. 13, p. 95, 2019. [5](#)
- [42] J. Liu, X. Fan, Z. Huang, G. Wu, R. Liu, W. Zhong, and Z. Luo, "Target-aware dual adversarial learning and a multi-scenario multi-modality benchmark to fuse infrared and visible for object detection," in *Proceedings of the IEEE/CVF Conference on Computer Vision and Pattern Recognition*, 2022, pp. 5802–5811. [5](#)
- [43] F. B. Campo, F. L. Ruiz, and A. D. Sappa, "Multimodal stereo vision system: 3d data extraction and algorithm evaluation," *IEEE Journal of Selected Topics in Signal Processing*, vol. 6, no. 5, pp. 437–446, 2012. [5](#)
- [44] D. P. Kingma and J. Ba, "Adam: A method for stochastic optimization," *arXiv preprint arXiv:1412.6980*, 2014. [5](#)
- [45] X. Wang, L. Xie, K. Yu, K. C. Chan, C. C. Loy, and C. Dong, "BasicSR: Open source image and video restoration toolbox," <https://github.com/XPixelGroup/BasicSR>, 2022. [5](#)
- [46] B. Lim, S. Son, H. Kim, S. Nah, and K. Mu Lee, "Enhanced deep residual networks for single image super-resolution," in *Proceedings of the IEEE conference on computer vision and pattern recognition workshops*, 2017, pp. 136–144. [6](#)
- [47] C. Dong, C. C. Loy, and X. Tang, "Accelerating the super-resolution convolutional neural network," in *Computer Vision—ECCV 2016: 14th European Conference, Amsterdam, The Netherlands, October 11–14, 2016, Proceedings, Part II 14*. Springer, 2016, pp. 391–407. [6](#)
- [48] C. Ledig, L. Theis, F. Huszár, J. Caballero, A. Cunningham, A. Acosta, A. Aitken, A. Tejani, J. Totz, Z. Wang *et al.*, "Photo-realistic single image super-resolution using a generative adversarial network," in *Proceedings of the IEEE conference on computer vision and pattern recognition*, 2017, pp. 4681–4690. [6, 7](#)
- [49] J. Liang, J. Cao, G. Sun, K. Zhang, L. Van Gool, and R. Timofte, "Swinir: Image restoration using swin transformer," in *Proceedings of the IEEE/CVF international conference on computer vision*, 2021, pp. 1833–1844. [6](#)
- [50] C. Dong, C. C. Loy, K. He, and X. Tang, "Image super-resolution using deep convolutional networks," *IEEE transactions on pattern analysis and machine intelligence*, vol. 38, no. 2, pp. 295–307, 2015. [6](#)

- [51] L. Sun, J. Pan, and J. Tang, “Shufflemixer: An efficient convnet for image super-resolution,” *Advances in Neural Information Processing Systems*, vol. 35, pp. 17 314–17 326, 2022. [6](#), [7](#)
- [52] X. Chen, X. Wang, J. Zhou, Y. Qiao, and C. Dong, “Activating more pixels in image super-resolution transformer,” in *Proceedings of the IEEE/CVF Conference on Computer Vision and Pattern Recognition*, 2023, pp. 22 367–22 377. [6](#), [7](#)